Vacancies and oxidation of two-dimensional group-IV monochalcogenides

Lídia C. Gomes, A. Carvalho, and A. H. Castro Neto

Centre for Advanced 2D Materials and Graphene Research Centre, National University of Singapore, 6 Science Drive 2, 117546, Singapore

(Received 15 April 2016; revised manuscript received 27 June 2016; published 9 August 2016)

Point defects in the binary group-IV monochalcogenide monolayers of SnS, SnSe, GeS, and GeSe are investigated using density functional theory calculations. Several stable configurations are found for oxygen defects, however, we give evidence that these materials are less prone to oxidation than phosphorene, with which monochalcogenides are isoelectronic and share the same orthorhombic structure. Concurrent oxygen defects are expected to be vacancies and substitutional oxygen. We show that it is energetically favorable for oxygen to be incorporated into the layers substituting for a chalcogen ($O_{S/Se}$ defects), and different from most of the other defects investigated, this defect preserves the electronic structure of the material. Thus, we suggest that annealing treatments can be useful for the treatment of functional materials where loss mechanisms due to the presence of defects are undesirable.

DOI: 10.1103/PhysRevB.94.054103

I. INTRODUCTION

Layered group-IV monochalcogenides have become an important group of materials within the ever-growing family of two-dimensional crystals. Among the binary IV-VI compounds, SnS, SnSe, GeS, and GeSe form a subgroup with orthorhombic structure belonging to the space group D_{2h}^{16}. Even though bulk structural, electronic and optical properties of these materials have been investigated since the 1970s [1–4], more recently their photovoltaic properties have been gaining considerable attention due to the increasing demand for efficient energy conversion technologies [5,6]. The optimal band gap for photovoltaic solar cells of the naturally occurring bulk SnS, also known as herzenbergite [7,8], boosted experimental and theoretical research on this material in recent years.

Additional interest in group-IV monochalcogenides arose with the advances in experimental techniques of production and manipulation of low-dimensional materials, paving an avenue for research in the two-dimensional (2D) field. While the most studied 2D materials are hexagonal, as graphene, phosphorene layers are orthorhombic [9], and therefore became a paradigm of anisotropy in two dimensions. Anisotropy has important consequences, for example, the enhanced thermoelectric effect arising from the fact that the preferential axes for heat and electronic conduction are orthogonal [10]. Monolayer group-IV monochalcogenides are isoelectronic with phosphorene and share the same structure, but have a lower symmetry, and therefore are expected to show large spin-orbit splitting [8] piezoelectricity and high ionic dielectric screening [11], all of them absent in phosphorene. Experimental progress in growth and exfoliation has already resulted in the isolation of bilayers, and the isolation of monolayer is expected [5,12,13].

In this article, we reveal yet another aspect in which group-IV monochalcogenides are more promising than phosphorene: their resistance to oxidation. In fact one of the hindrances to the research and use of phosphorene is its tendency to oxidize [9,14]. Exposed to air, few-layer samples degrade in less than one hour [15], eventually producing phosphorus oxide and phosphoric acid. Thus, phosphorene devices require immediate encapsulation in order to maintain their I-V characteristics [16,17]. However, group-IV chalcogenides have stronger bonds and therefore are expected to be less prone to oxidation. In this article, we use first-principles calculations to investigate point defects in group-IV monochalcogenide monolayers. Section III A is dedicated to the study of chemisorbed oxygen defects. Subsequently, in Sec. III B we study the effects of intrinsic vacancy defects and substitutional oxygen. Conclusions are presented in Sec. IV.

II. METHODS

We use first-principles calculations based on density functional theory to obtain the electronic and structural properties of oxidized monolayer monochalcogenides. We employ a first-principles approach based on Kohn-Sham density functional theory (KS-DFT) [18], as implemented in the QUANTUM ESPRESSO code. [19]. The exchange correlation energy was described by the generalized gradient approximation (GGA) using the PBE [20] functional. Interactions between valence electrons and ionic cores are described by Troullier-Martins pseudopotentials [21]. The Kohn-Sham orbitals were expanded in a plane-wave basis with a cutoff energy of 70 Ry, and for the charge density, a cutoff of 280 Ry was used. The Brillouin zone (BZ) was sampled using a Γ-centered $10\times10\times1$ grid following the scheme proposed by Monkhorst and Pack [22].

We used periodic boundary conditions along the three dimensions. The layers are placed in the x-y plane, with the y axis parallel to the puckering direction, where atoms are arranged in a zigzag shape. Along the perpendicular x axis, the atoms form an armchair configuration. In direction perpendicular to the layers, we used vacuum regions of 10 Å between adjacent images. Convergence tests with greater vacuum thickness were performed, and the values used are enough to avoid spurious interaction between neighboring images.

The isolated defects were modeled using 3×3 supercells ($M_{18}C_{18}$, with M = Sn,Ge and C = S,Se). The unit cells with an adsorbed oxygen atom have, therefore, $M_{18}C_{18}O$ chemical composition, while for vacancies and O substitutional the concentrations are $M_{18(17)}C_{17(18)}$ and $M_{18(17)}C_{17(18)}O$, respectively.

III. RESULTS

A. Oxygen defects

1. Crystal structure and energetics

Group-IV monochalcogenides are isoelectronic with phosphorus. Their monolayer form assumes a corrugated structure very similar to phosphorene, with all atoms threefold coordinated (Fig. 1). The presence of two atomic species lowers the symmetry, and thus the bulk structure belongs to the space group $Pnma$-D_{2h}^{16}, while black phosphorus is $Pnma$-D_{2h}^{18}. In the monolayer form, they also lose inversion symmetry in the perpendicular direction of the layers, which places them in the $Pn2_1m$-C_{2v}^{7} space group.

Oxygen atoms can be adsorbed at numerous different positions. As an initial step, we consider six configurations for isolated oxygen defects, derived from the models for oxygen defects in phosphorene considered in Ref. [9]. The models can be divided into dangling, horizontal bridge (HB), and interstitial bridge (IB) configurations, and are shown in the first column in Figs. 2 and 3.

In dangling oxygen configurations the oxygen atom is bonded to only one lattice atom, borrowing two electrons from one of the lone pairs of C or M. Thus, in group-IV monochalcogenides there are two distinct dangling bond configurations. These models are labeled O-$M(C)$-MC, where $M(C)$ = Sn, Ge (S, Se) indicates the species oxygen is bonded to. The two dangling oxygen structures are shown in Figs. 2(a) and 2(b).

We also consider two horizontal bridge configurations consisting of one oxygen positioned midway between two Sn(Ge) atoms of either two neighbor zigzag (ZZ) chains [i.e., along the armchair (AC) direction], or the same zigzag chain, along the zigzag direction. These models are labeled O-HB-AC-MC and O-HB-ZZ-MC and are shown in Figs. 2(c) and 2(d), respectively. In the bridge-type configurations the oxygen forms two single bonds to its nearest neighbors.

In the interstitial configurations the oxygen is initially placed at a bond center, i.e., between a M and C atom. The bonds can be aligned perpendicular to the layer plane, when it is formed between atoms located at different sublayers, or parallel to the layer plane, with bonds between atoms within the same sublayer. These models are named O-IB-pp-MC and O-IB-pa-MC, respectively, and are shown in Figs. 3(a) and 3(b).

For all defects, the six initial structures (first column in Figs. 2 and 3) give rise to the respective optimized structures presented in columns 2–5 for SnS, SnSe, GeS, and GeSe. The four materials show some variation in the final structures. After optimization, most defects result in significant distortion of the

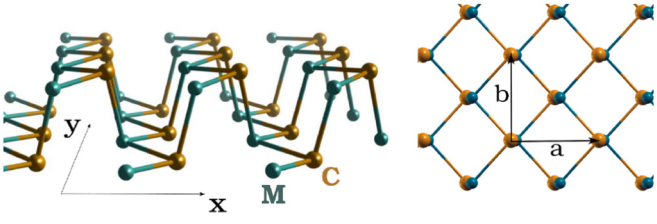

FIG. 1. Structure and lattice parameters of the pristine layers. The chemical composition of the pristine material is MC, with M = (Sn, Ge) and C = (S, Se).

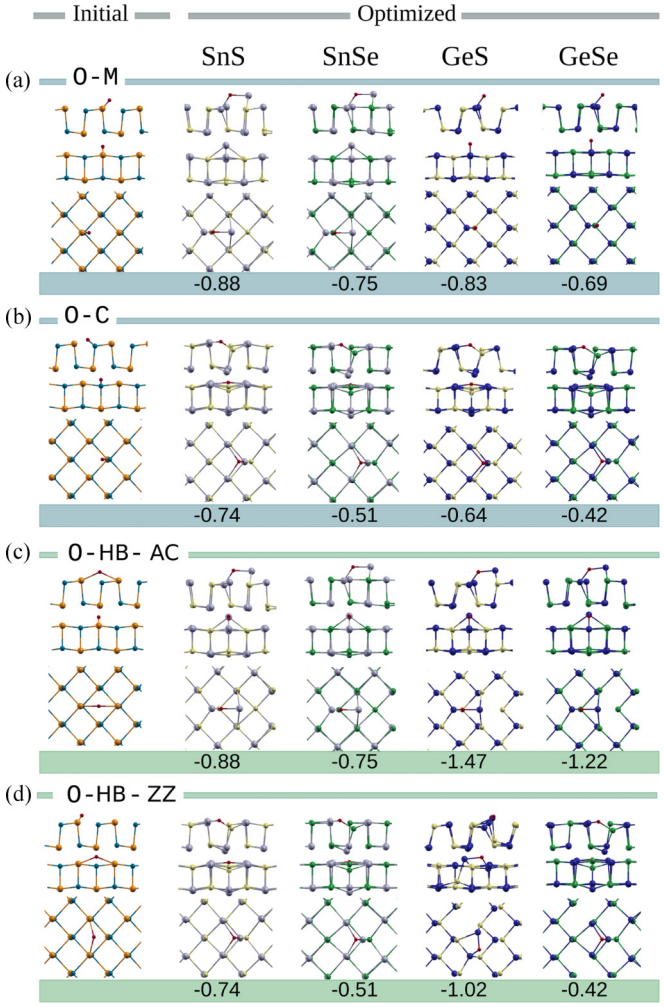

FIG. 2. Structures of chemisorbed oxygen defects, where M = (Sn, Ge) and C = (S, Se). The initial positions of the oxygen atoms (in red) are shown in the first column for the different models. The coordinate axes used in all systems are shown in the first row. The six different O positions are labeled: (a), (b) dangling oxygen defects (O-M and O-C); (c), (d) horizontal bridge defects, one with O bonds parallel to the armchair x direction (O-HB-AC), and one with O bonds along the zigzag y direction (O-HB-ZZ). Two interstitial oxygen (Fig. 3) are also discussed. The optimized layers for SnS, SnSe, GeS, and GeSe are depicted in columns 2–5.

MC structure in their neighborhood. Exceptions are dangling oxygen defects bonded to Ge in GeS and GeSe, for which the lattice remains little changed.

In addition, not all structures are stable for all four materials. Take as an example the SnS oxygen defects. In the horizontal bridge configuration O-HB-AC-SnS, oxygen atoms are initially bonded to two Sn atoms at equal distances O − Sn $\simeq$ 2.3 Å. After optimization, oxygen pulls one of the Sn atoms to $h_{\text{out}}^{\text{top}} = 0.80$ Å above the monolayer plane and along x direction, towards to the second atom bonded to O. This is exactly the same structure adopted by the dangling oxygen O-Sn-SnS after optimization, as can be seen in Fig. 2(a). The dangling oxygen and bridge oxygen configurations, O-S-SnS and O-HB-ZZ-SnS, assume also very similar structures after optimization, with the lattices less affected by the introduction

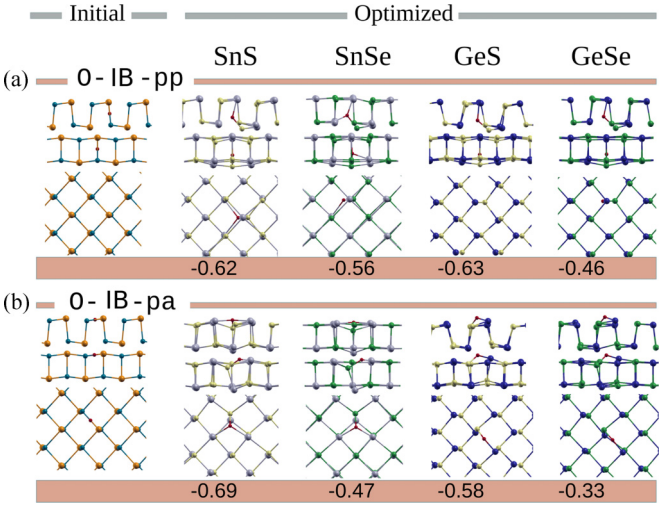

FIG. 3. Interstitial oxygen models O-IB-pp and O-IB-pa for oxygen placed between atoms located at different sublayers and within the same sublayer, respectively. The coordinate axes used in all systems are shown in the first row. The optimized layers for SnS, SnSe, GeS, and GeSe are depicted in columns 2–5.

of the oxygen atom. In this case, the sulfur in the O-S bond is pulled into the layer by about $h_{\text{in}} = 0.37$ Å while the tin atom directly below it is pushed $h^{\text{bot}}_{\text{out}} = 0.30$ Å out of the bottom layer surface. For SnSe, the initial O-Sn and O-HB-AC models also adopt the same final structures, as well O-Se and O-HB-ZZ. The structural parameters $h^{\text{top}}_{\text{out}}$, h_{in}, and $h^{\text{bot}}_{\text{out}}$ for all materials are shown in Table I.

Different results are found for GeS and GeSe. For these materials, the dangling O-Ge and horizontal bridge O-HB-AC models do not adopt the same final structure, as observed for SnS and SnSe. This result comes essentially from the different lattice parameters **a** of the layers along the x direction and very different covalent radius of the atomic species. As shown in Table II, the GeS and GeSe lattice parameters along x are larger than in SnS. In the case of dangling O-Ge, this results in the oxygen being initially slightly farther from the Ge atom at the adjacent zigzag chain, hindering their interaction. In this case, there is no appreciable deformation of the structures due to the lack of a second O-Ge bond, and the O-Ge-GeS/GeSe models reaches the local minima shown in Fig. 2(a). For SnSe, the larger lattice along x (in comparison to GeSe) is compensated by the bigger covalent radius of Sn, allowing the formation of the second O-Sn bond.

The main effect of the interstitial oxygen in the O-IB-pp and O-IB-pa models is to push the M and C atoms bonded to it outside of the monolayer plane, in order to accommodate larger O-M and O-C bonds. For most of the optimized structures of these two models, oxygen retains the two initial bonds. Exceptions are O-IB-pa in SnS and SnSe, where one additional O-Sn bond is formed with the second Sn neighbor, due to the larger covalent radius of tin.

Along with an analysis of the structural changes, we investigate the energetic stability of the oxidized materials. The binding energy E_b per oxygen atom is defined as:

$$E_b = E_{l+\text{O}} - (E_l + N_{\text{O}}\mu_{\text{O}}), \tag{1}$$

where $E_{l+\text{O}}$ is the total energy of the defective layers, E_l is the energy of the pristine layers (without the adsorbed oxygen), μ_{O} is the chemical potential of oxygen, and N_{O} is the number of oxygen atoms per unit cell, which we choose as $N_{\text{O}} = 1$ in this work. A natural choice for μ_{O}, is the chemical potential of O_2 molecules as the oxygen source, from which μ_{O} is obtained by $E_{\text{O}_2}/2$, where E_{O_2} is the total energy of the O_2 molecule. Defined as in Eq. (1), a negative E_b indicates that the defect formation is energetically favorable (exothermic reaction). The calculated E_b for all materials and defect models are presented in Table III.

Most of the materials within the different models present relatively low oxygen binding energies, with values ranging from −0.33 eV to −0.88 eV. The Ge chalcogenides have the two highest oxygen binding energies: −1.47 eV for GeS and −1.22 eV for GeSe, both for the optimized O-HB-AC model. This indicates that GeS and GeSe are the most susceptible

TABLE I. Structural parameters (in Å) for the optimized structures.

	$h^{\text{top}}_{\text{out}}$	h_{in}	$h^{\text{bot}}_{\text{out}}$	$h^{\text{bot}}_{\text{out}}$ (O-IB-pp)
SnS	0.80	0.37	0.30	0.70
SnSe	1.52	0.68	0.57	0.61
GeS	1.33	0.40	0.37	0.56
GeSe	1.60	0.74	0.62	0.51

TABLE II. Theoretical and experimental lattice parameters (in Å) of SnS, SnSe, GeS, GeSe. The theoretical results include van der Waals effects for bulk. Experimental data for bulk SnS and SnSe are also presented.

		Monolayer		Bulk			
		a	b	c	b	c	
SnS	Theory	4.24	4.07	4.27	4.00	11.12	This work.
	Expt.	-	-	4.33	3.98	11.20	[23,24]
SnSe	Theory	4.36	4.30	4.47	4.20	11.58	This work.
	Expt.	-	-	4.44	4.15	11.50	[25]
GeS	Theory	4.40	3.68	4.34	3.67	10.41	This work.
GeSe	Theory	4.26	3.99	4.39	3.90	10.93	This work.

TABLE III. Binding energies E_b (eV) for chemisorbed oxygen atoms in monolayer monochalcogenides. For SnS and SnSe: (*) same as O-M, (**) same as O-C.

	SnS	SnSe	GeS	GeSe
O-M	−0.88	−0.75	−0.83	−0.69
O-C	−0.74	−0.51	−0.64	−0.42
O-HB-AC	−0.88 *	−0.75 *	−1.47	−1.22
O-HB-ZZ	−0.74 **	−0.51 **	−1.02	−0.42
O-IB-pp	−0.62	−0.56	−0.63	−0.46
O-IB-pa	−0.69	−0.47	−0.58	−0.33

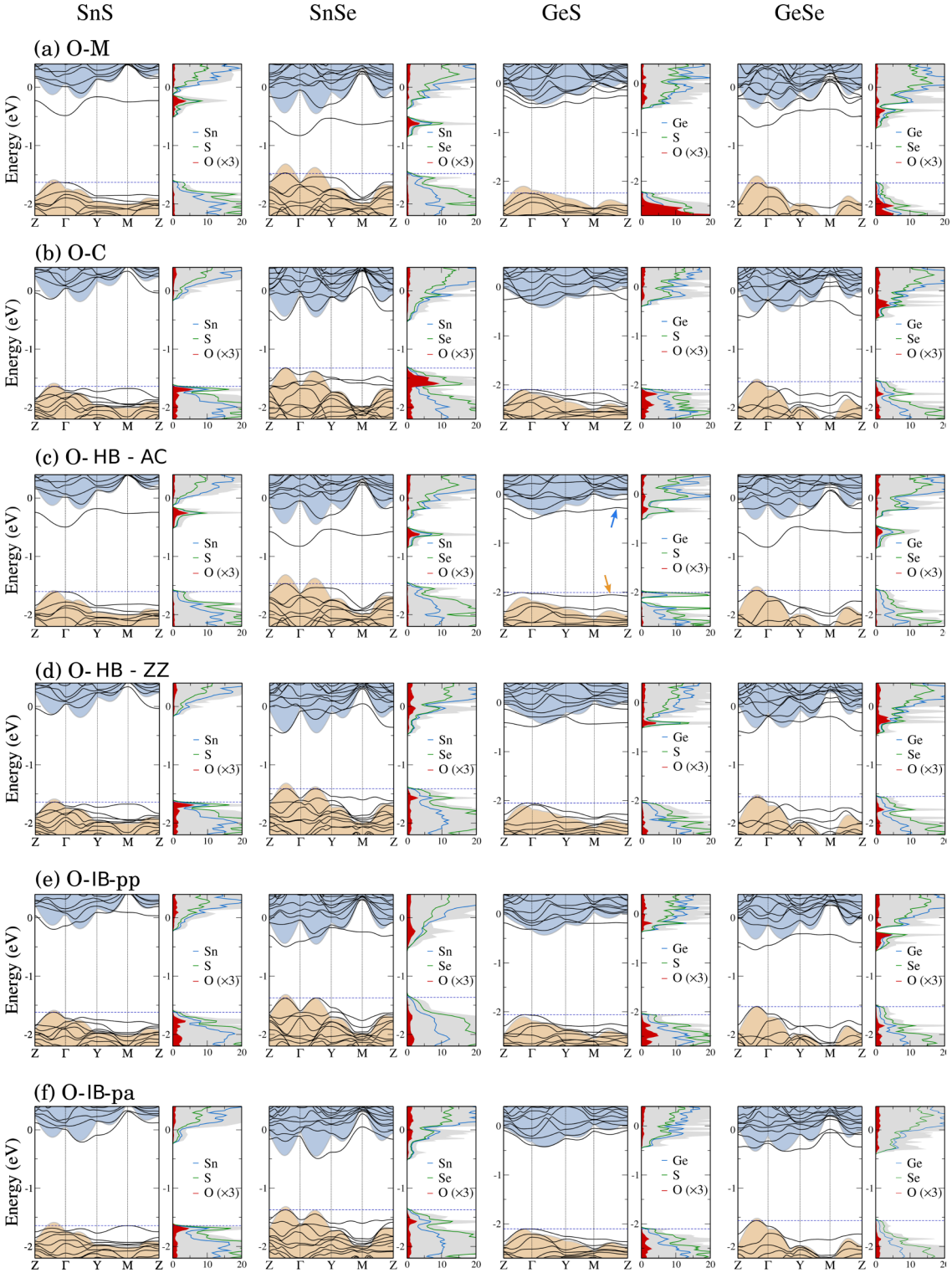

FIG. 4. Electronic bands, total and partial DOS for (a) O-*M* and (b) O-*C* dangling oxygen, (c) O-HB-AC and (d) O-HB-ZZ horizontal bridge oxygen, and (e) O-IB-pp and (f) O-IB-pa interstitial oxygen. For comparison, the electronic bands of a 3×3 pristine unit cell are overlayed to the band structures, with the valence bands in light orange and the conduction bands in light blue. The Fermi level is marked by a horizontal dashed line. The bands are shown in the same order as the corresponding relaxed structures in Fig. 2. All the bands are aligned with the vacuum level at 0 eV.

to oxidation. Even in this case, the absorption energy is still lower than in phosphorene, where the binding energy for the dangling configuration is found to be -2.08 eV using a similar method.

Overall, comparing the energies of the different defects across the four materials (Table III), we find that the lowest energy configuration is always the horizontal bridge oxygen along the armchair direction, O-HB-AC.

2. *Electronic properties*

Figure 4 shows the electronic band structures for all oxygen defect configurations. The total density of states (DOS) and the contribution of each atomic specie to the electronic states, i.e., the projected density of states (PDOS), are also presented. The DOS of oxygen is multiplied by three, to facilitate visualization. The electronic properties of monolayer monochalcogenides are appreciably affected by the introduction of oxygen. The characteristic valleys observed for the pristine structures [8] are strongly modified when they are exposed to oxygen, due to hybridization with O atoms.

Let us first concentrate on the low-energy horizontal bridge O-HB-AC defect configuration [Fig. 4(c)]. Empty level states are introduced in the gap at 0.53 eV (SnS), 0.80 eV (SnSe), 0.17 eV (GeS), and 0.71 eV (GeSe) below the pristine conduction band at the Γ point of the Brillouin zone (BZ). In GeS, an occupied state is also formed 70 meV above the top of the pristine valence band at Γ. Figure 5 shows the charge density contribution of the defective in-gap states in GeS.

From Fig. 5(a) we see that the highest occupied band [pointed out by the orange arrow in Fig. 4(c)] is mainly formed by the states of the lone pair of the S atoms, which lose the bond with Ge. The empty level introduced in the gap [pointed out by the blue arrow in Fig. 4(c)] is an antibonding state formed between one of the M atoms bonded to oxygen and its first neighbors, as shown in Fig. 5(b). This is the same nature of the empty states introduced in SnS, SnSe, and GeSe.

The horizontal bridge defects O-HB-ZZ-MC, in contrast, do not introduce gap states and are, therefore, electrically neutral for all materials.

The electronic bands, total and partial density of states for the monolayers with dangling oxygen configurations are presented in Figs. 4(a) and 4(b). When the oxygen is bonded to a chalcogen atom (O-C structures), no gap states are introduced. On the other hand, when oxygen is bonded to a group-IV atom (O-M structures), the conduction band is perturbed and acceptor levels are introduced. The gap state is localized mainly on the Sn or Ge atoms directly bonded to the oxygen.

For the interstitial bridge defects, O-IB-pp and O-IB-pa, the top of the valence band is less affected than in the other defect models for most of the materials. On the other hand, the conduction bands are strongly modified in comparison to the pristine layers. In particular, for GeSe with the O-IB-pp defect, an acceptor state is formed a few meV below the conduction band minimum.

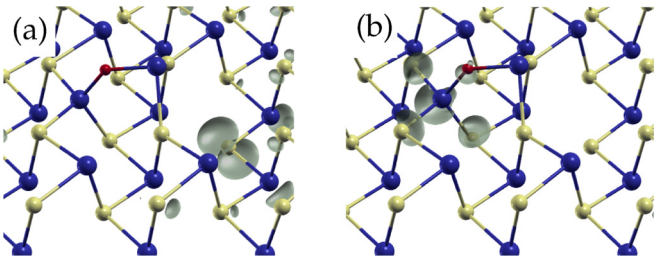

FIG. 5. Charge density contribution to the defective states in O-HB-AC model in GeS. We show (a) the contributions to the highest occupied state and (b) lowest unoccupied state. These states are indicated by the orange and blue arrows in Fig. 4(c). The charge density distributions for the other compounds (SnS, SnSe, and GeSe) are very similar and are not shown for simplicity.

Activation energies can be estimated by the marker method (MM), as detailed in Ref. [26]. This method allows us to estimate energy levels comparing ionization energies of defective systems in different charge states, referent to a known marker system. A natural choice as reference system is the pristine (undefective) material, when other appropriate markers, for which reliable experimental data exists, are not available. With these considerations, it is shown [26] that the electrical levels of an unknown system can be defined with respect to a known marker system by means of their total energies. We need to emphasize that the MM is more reliable for comparison between chemically (and structurally) similar systems. In the case of 2D materials modeled with periodic boundary conditions, the marker method is an efficient way to cancel, in a good approximation, the energy resulting from the spurious electrostatic interaction between neighboring cells [27].

For the models discussed up to now, we focus on calculate activation energies for the O-M and low-energy O-HB-AC systems, which present in-gap defective acceptor bands for all the monochalcogenides investigated here. The activation energies of the defective states are calculated from the differences in electron affinities:

$$I_D - I_m = [E_D(0) - E_D(q)] - [E_m(0) - E_m(q)], \qquad (2)$$

where $E(q)$ is the energy of the supercell in charge state $q = \{-,+\}$, and the subindices $m(D)$ refer to pristine (defective) systems. Charged systems with an extra electron ($q = -1$) or a missing electron ($q = +1$) are considered for the pristine and defective monolayers with acceptor or donor states, respectively. The total energies used in Eq. (2) are computed from GGA-PBE exchange-correlation functional. The calculated results are summarized in Table IV.

All acceptor levels are deep, lying in the upper half of the band gap. The O-HB-AC defect in GeS presents the shallower state, with activation energy of 50 meV. GeS is also the only material that presents a donor defective state. Such a state is deep, with an activation energy of 100 meV.

B. Vacancies and substitutional oxygen

Besides the adsorbed oxygen discussed in the previous section, intrinsic defects are another class of dominant defects

TABLE IV. Activation energies (in eV) of the defects in O-M and O-HB-AC adsorbed oxygen systems and of the chalcogen vacancies V_C. For the adsorbed O models, the acceptor levels $(-/0)$ are deep and located in the upper half of the band gap. The V_C vacancies present donor states $(0/+)$ only for sulfides, being shallower in GeS than in SnS.

	SnS	SnSe	GeS	GeSe	
O-M	0.17	0.31	0.11	0.22	$(-/0)$
O-HB-AC	0.17	0.31	0.05	0.33	$(-/0)$
	-	-	0.10	-	$(0/+)$
V_C	0.21	-	0.07	-	$(0/+)$

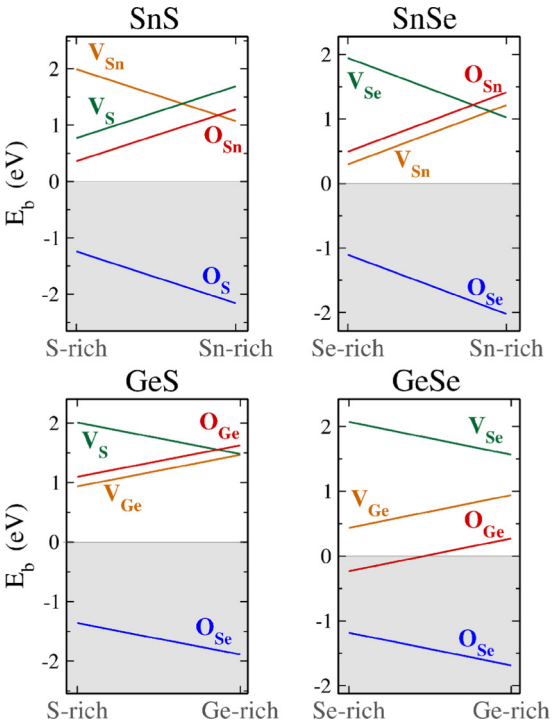

FIG. 6. Formation energies E_f (eV) for vacancies and substitutional oxygen defects for M-rich (M = Sn, Ge) and C-rich (C = S, Se) conditions. All the vacancies present positive formation energies, an indication that their formation process is endothermic. On the other side, oxygen substitutional at the chalcogen sites (O_S and O_{Se} defects), are energetically favorable to occur in these systems, given their remarkable negative E_b values.

present in 2D materials. Bulk SnS, for instance, is characterized by an intrinsic p-type conductivity due to typical acceptor states formed by Sn vacancies (V_{Sn}) [28]. S vacancies (V_S) can also be formed under appropriate Sn-rich conditions as well as substitutional oxygen at S sites (O_S). Experimental studies also indicate the presence of vacancies in single-crystal GeSe nanosheets, and discuss the role of the resulting defective states in the photoresponse of this material [5]. In this section, we investigate intrinsic defects in the monolayers of group-IV monochalcogenides. We discuss the energetic of the systems with introduction of four different types of defects: two vacancies, V_M and V_C, and two substitutional oxygen defects, O_M and O_C.

Formation energies (E_f) are calculated using

$$E_f = E_{\text{def}} - (N_M\mu_M + N_C\mu_C + N_O\mu_O), \qquad (3)$$

where E_{def} is the total energy of the defective structure, μ_i and N_i are the chemical potential and number of atoms of i type. The chemical potentials for M and C (μ_M and μ_C, respectively) for Ge and Sn-rich conditions are taken from the diamond structure of these elements. The chemical potentials for Se- and S-rich environments are calculated using the molecular crystal ($R\bar{3}$ phase) Se_6 and the S_8 molecule [29]. The formation energy (E_f) interval is presented in Fig. 6, where, as in the previous section for the binding energy, our definition of formation energy yields negative values for exoenergetic processes.

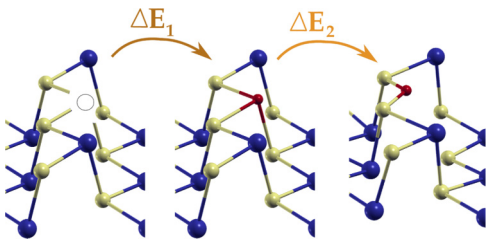

FIG. 7. Schematic for contributions of energy gain for introduction of oxygen into a vacancy site ($V_{S/Se} + \frac{1}{2}O_2 \rightarrow O_{S/Se}$ reaction). $\Delta E_1 = \overline{E}^{V+O}_{\text{total}} - (\overline{E}^{V}_{\text{total}} + \mu_O)$ and $\Delta E_2 = E^{V+O}_{\text{total}} - \overline{E}^{V}_{\text{total}}$. $\overline{E}$ indicates that the total energy is given with reference to a nonoptimized structure.

The defect formation energies at $T = 0$ calculated in this way do not take into account zero-point energies, or the contributions of vibrational entropy and configurational entropy and $T > 0$. This is an approximation commonly adopted in defect studies and that usually results in a small, systematic error that partially cancels out when comparing similar defects (usually, the total zero-point and entropic contribution to the free energy gives rise to changes of less than 0.2 eV below 800 K, see Refs. [30–33]). For example, for some carbon-containing defects in silicon (note that carbon is lighter than oxygen), the zero-point energy can be as low as 65 meV or less [31].

The first marked result is the indication of stability of all O-substitutional defects at the chalcogen sites, given by the negative values of the O_S and O_{Se} defects. In addition to $O_{S/Se}$, the only defect model that presents negative formation energy is the O_{Ge} in GeSe, under Se-rich condition. All vacancies, as well the remainder substitutional oxygen $O_{Sn/Ge}$, are endothermic processes and, at least in the growth environments considered here, should not be favorable to occur in the single layer of these materials.

Formation energies of vacancies and oxygen substituting for Sn/Ge are positive, however, the formation energies of oxygen replacing S/Se are negative. Thus, the reaction $V_{S/Se} + \frac{1}{2}O_2 \rightarrow O_{S/Se}$ is energetically favorable.

We can gain more information on the contribution of structural relaxation on the formation energy of substitutional oxygen. To this end, we separate the change in total energy after oxygen is absorbed into a vacancy site but before structural relaxation (ΔE_1), and after relaxation of the atomic coordinates (ΔE_2), as represented in Fig. 7. The calculated ΔE_1 and ΔE_2 are shown in Table V, where negative (positive) values indicate lowering (rising) in energy.

We see that the robust stability of the O_C defects, from a $V_{S/Se} + \frac{1}{2}O_2 \rightarrow O_{S/Se}$ reaction, comes from contributions of

TABLE V. Energy gain for formation of substitutional oxygen from vacancies and structural optimization.

		SnS	SnSe	GeS	GeSe
$V_M + O$	ΔE_1	2.77	2.57	2.10	1.96
	ΔE_2	−3.70	−2.77	−2.46	−3.01
$V_C + O$	ΔE_1	−2.06	−1.27	−2.19	−1.35
	ΔE_2	−1.50	−2.11	−1.62	−2.27

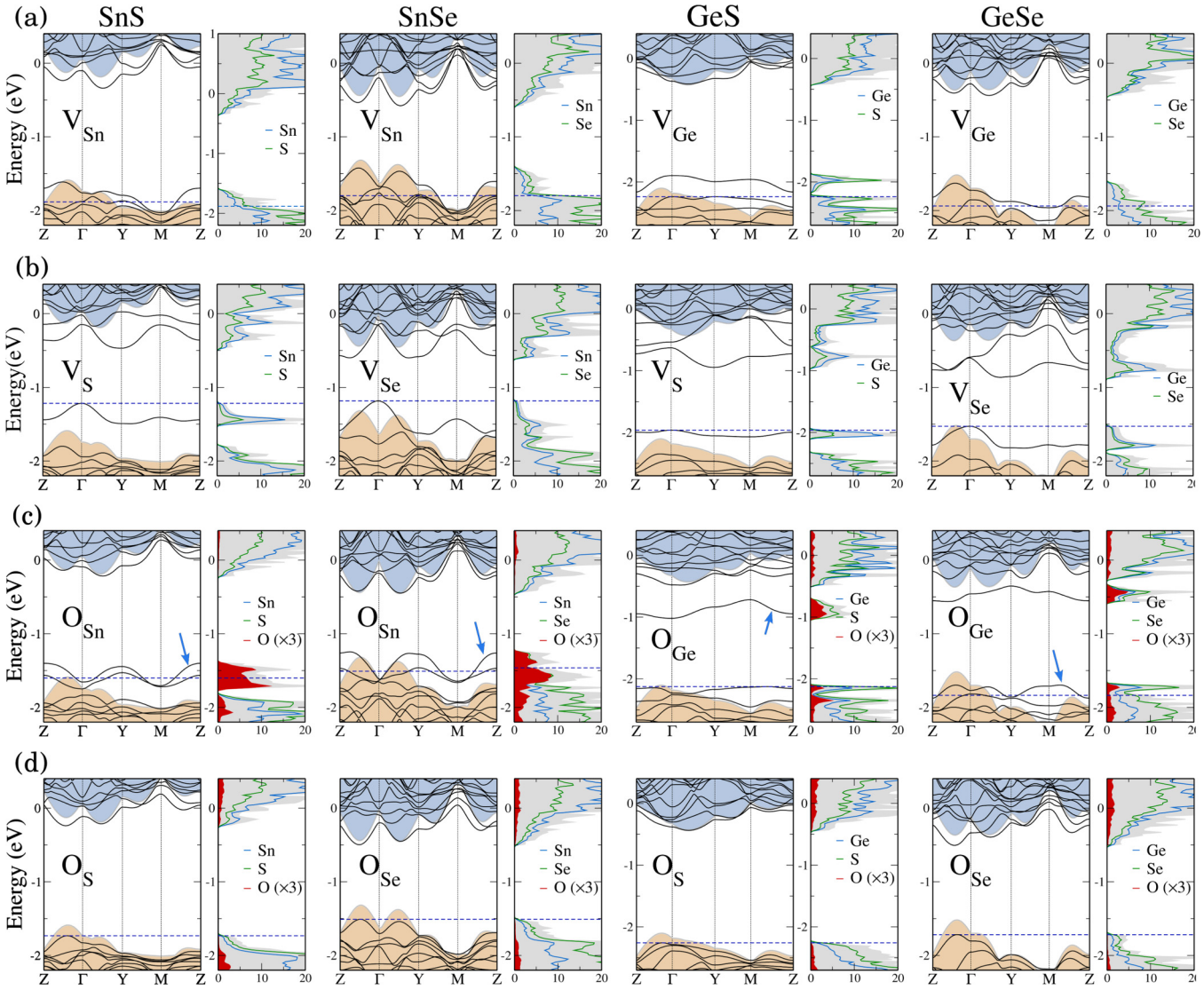

FIG. 8. Electronic bands, DOS and PDOS for monolayers with (a) vacancies of group-IV elements (Sn, Ge), (b) vacancies of chalcogens (S, Se), (c) substitutional O defects in group-IV elements (Sn, Ge), and (d) substitutional O defects in chalcogen atoms (S, Se). For comparison, the electronic bands of a 3×3 pristine unit cell is overlayed to the band structures, with the valence bands in light orange and the conduction bands in light blue. The Fermi level is marked by a horizontal dashed line. All the bands are aligned with the vacuum level at 0 eV.

both oxygen passivation and structural relaxation processes. While the former is the largest for the sulfides, the latter is the largest for selenides. In the formation process of O_M defects, all materials experienced an appreciable increasing in energy upon incorporation of oxygen at V_M sites. The reduction in energy comes essentially from structural deformation, which is more effective in SnS and GeSe, providing the formation energies of O_M be lower than V_M in these materials rather than in SnSe and GeS.

Electronic properties

Inspection of the electronic structure of the different types of vacancy defects indicates that Sn/Ge vacancies remove valence states, acting as shallow acceptors and displacing the Fermi level below the valence band top, as shown in Fig. 8(a). In the case of chalcogen vacancies, perturbed valence and conduction bands appear in the selenides. A similar perturbed state has been predicted for bulk GeSe with the same type of defect [5]. For the sulfides, S vacancies introduce deep donor states, localized at Sn and Ge atoms in the vicinity of the missing S atom. Activation energies of the V_S states are presented in Table IV and show that the defect state is shallower in GeS (70 meV) than in SnS (210 meV).

The electronic bands for substitutional oxygen defects are presented in Figs. 8(c) and 8(d) for substitution at Sn/Ge and S/Se sites, respectively. We first discuss the $O_{Sn/Ge}$ case. As a result of the considerable difference in size between oxygen and Sn/Ge atoms, which are bigger by 93%/67%, the monolayers with $O_{Sn/Ge}$ defects are not stable: oxygen moves from its initial position forming one, two or three bonds in the optimized structures, as shown in Fig. 10. Despite the higher valence of oxygen (s^2p^4) in relation to Sn and Ge (s^2p^2), its smaller size compared to these group-IV atoms,

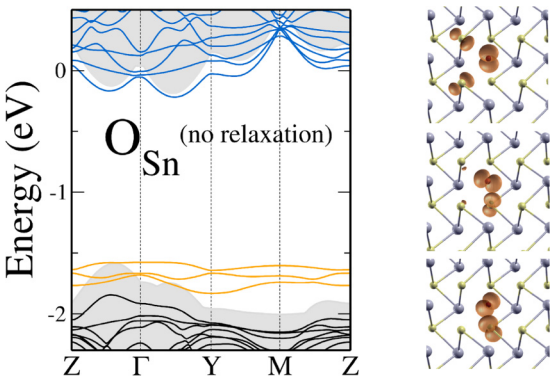

FIG. 9. Electronic bands of nonoptimized SnS monolayer with a O_{Sn} intrinsic defect. In addition to the fully occupied and unoccupied bands (in black and blue colors), three partially filled states (in orange) are introduced at the top of the valence bands. These bands are composed by a considerable contribution of oxygen p states, as shown by the charge density surface at the right. The bands are aligned with the vacuum level at 0 eV. For comparison, the electronic bands of a 3×3 pristine unit cell is overlayed (in light gray) to the band structures.

gives a vacancy character to the $O_{Sn/Ge}$ defects. As a result, the electronic structures show shallow acceptor levels in all cases except GeS, where it introduces a deep state instead [Fig. 8(c)]. This vacancy character given by substitutional oxygen at atomic sites of originally lower valence has been found for other materials. Examples are O_C defects in diamond [34], O_{Ga} in GaN [35] and the well-known vacancy-oxygen defect in silicon [36].

We can analyze more carefully the origin of these acceptor levels starting by looking at the structural and electronic features of the substitutional oxygen defects of the nonoptimized structures. As an example, we consider the O_{Sn} defect in SnS. The small covalent radius of oxygen makes it to be initially very weakly bonded to its neighboring sulfur atoms (Fig. 9). Three states with oxygen atomiclike character are introduced near to the top of the valence bands, corresponding to partially occupied p orbitals. After optimization, oxygen moves towards one of the sulfur atoms, bonding to it [Fig. 10(a)], and thus lowering the energy of the p_z orbital, which strongly hybridizes with Sn and S states. The two acceptor states are formed by a strong contribution of the half-filled p_x and p_y oxygen states. The same process occurs for SnSe [Fig. 10(b)].

In GeS, the substitutional oxygen bonds to the two upper S atoms, fully filling its p orbitals. A deep antibonding state is formed below the conduction band (at ≈ -1 eV). Such state is empty and highly localized on the oxygen and sulfur atoms bonded to oxygen, as shown by the charge density distribution of the defect state, plotted in Fig. 10(c). For GeSe, the optimized O_{Ge} defect evolves to a configuration where oxygen is bonded to the two nearest Ge atoms at the bottom layer and to a S atom, in a sp^2 hybridization. An acceptor state is formed just above the top of the valence bands. This state is composed mainly by the remainder empty p_z oxygen orbital and by an antibonding state partially located on the Se closest to the O, as shown in Fig. 10(d). Similarly to GeS, an empty band is introduced below the bottom of the conduction bands

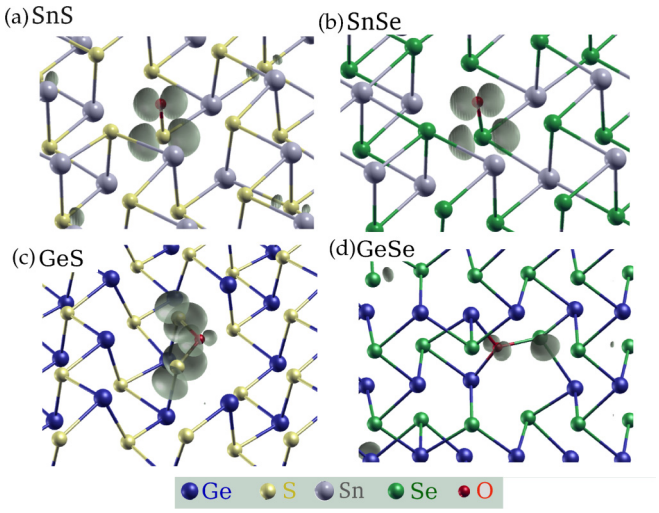

FIG. 10. Isosurface of charge density for the first unoccupied band in monolayers with substitutional O_M defect. For SnS, SnSe, and GeSe, such bands are located crossing or slightly above the Fermi level, while for GeS, it is represented by the deep state below the bottom of the conduction bands. These bands are identified by blue arrows in Fig. 8(c). The plots show the localized nature of the bands in the region around the oxygen.

(at ≈ -0.5 eV), which is composed mainly by an antibonding state from the O-Se bond.

The size mismatch is smaller between oxygen and the chalcogens S and Se, resulting in less distorted structures for layers with $O_{S/Se}$ defects (Fig. 11). In addition, substitutional $O_{S/Se}$ are isoelectronic with the pristine structure and do not introduce gap states for most of the compounds, as shown in Fig. 8(d), leaving the band structure nearly unaffected.

Given the lack of experimental results on the properties of monolayer monochalcogenides, we establish a comparison with bulk and few-layer material. In Ref. [5], photoresponse analysis of single-crystal GeSe nanosheets shows a slow decay time, which is attributed to defect states created in the samples upon chemical process or light and heat application in the

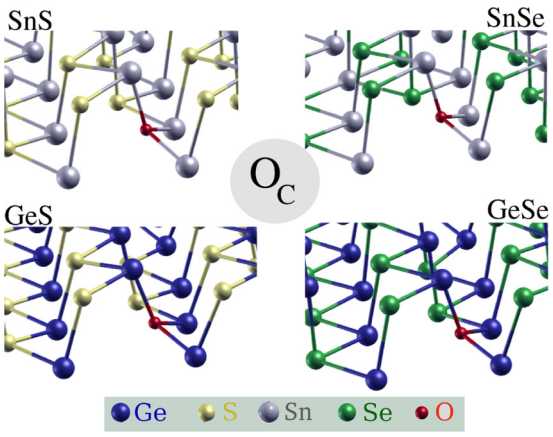

FIG. 11. Optimized structures of monolayers with substitutional oxygen at chalcogen sites O_C, C = (S, Se). The layers are less distorted for this defect due to the small lattice mismatch between oxygen and sulfur and selenium atoms.

fabrication process. In the same work [5], first-principles calculations of defects in bulk GeSe show the presence of middle gap states for vacancies and interstitial atoms. The energetic preference of oxygen to be incorporated into the layers, occupying the chalcogen sites (S and Se atoms), at the two limits of chemical potentials has also been reported by a previous study of surface passivation of bulk SnS [37].

IV. CONCLUSIONS

Point defects in group-IV monochalcogenides monolayers—SnS, SnSe, GeS, and GeSe—are investigated using first-principles density functional theory calculations. Energetic and structural analysis of five different models for chemisorbed oxygen atoms reveals a better resistance of these materials to oxidation if compared to their isostructural partner, phosphorene. Among all monochalcogenides, GeS is the most prone to oxidation, as it presents larger binding energies for four of the five models investigated.

Electronic structure calculations show that the most stable oxygen configurations have deep acceptor states, and so do the chalcogen vacancies. However, oxygen substitution leads to neutral defects, which preserve the electronic structure of the pristine material. Substitutional oxygen forms spontaneously at the chalcogen sites in the presence of chalcogen vacancies and oxygen. This indicates that annealing/laser healing of vacancy defects will be effective in removing gap states in group-IV monochalcogenides, as was found for TMDCs [38,39].

In contrast, Sn/Ge vacancies are shallow acceptors, and therefore are expected to confer *p*-type character to chalcogen-rich material. In this case, annealing in oxygen is not expected to be an effective passivation technique.

ACKNOWLEDGMENTS

This work was supported by the National Research Foundation-Prime Minister's Office, Republic of Singapore, under its Medium Sized Centre Programme and CRP award "Novel 2D materials with tailored properties: beyond graphene" (Grant No. R-144-000-295-281). The first-principles calculations were carried out on the GRC high-performance computing facilities.

[1] R. Eymard and A. Otto, Optical and electron-energy-loss spectroscopy of GeS, GeSe, SnS, and SnSe single crystals, Phys. Rev. B **16**, 1616 (1977).

[2] P. C. Kemeny, J. Azoulay, M. Cardona, and L. Ley, Photoelectron spectra of GeS, GeSe, SnS and SnSe and their relation to structural trends and phase transitions within the average-valence-5 compounds, Il Nuovo Cimento B **39**, 709 (1977).

[3] H. Wiedemeier and H. G. von Schnering, Refinement of the structures of GeS, GeSe, SnS and SnSe, Z. Kristallogr. **148**, 295 (1978).

[4] M. Parenteau and C. Carlone, Influence of temperature and pressure on the electronic transitions in SnS and SnSe semiconductors, Phys. Rev. B **41**, 5227 (1990).

[5] B. Mukherjee, Y. Cai, H. R. Tan, Y. P. Feng, E. S. Tok, and C. H. Sow, NIR Schottky photodetectors based on individual single-crystalline GeSe nanosheet, ACS Appl. Mater. Interfaces **5**, 9594 (2013).

[6] A. M. Cook, B. M. Fregoso, F. de Juan, and J. E. Moore, Design principles for shift current photovoltaics, arXiv:1507.08677.

[7] A. Walsh and G. W. Watson, Electronic structures of rocksalt, litharge, and herzenbergite SnO by density functional theory, Phys. Rev. B **70**, 235114 (2004).

[8] L. C. Gomes and A. Carvalho, Phosphorene analogues: Isoelectronic two-dimensional group-IV monochalcogenides with orthorhombic structure, Phys. Rev. B **92**, 085406 (2015).

[9] A. C. Ziletti, A. Carvalho, D. K. Campbell, D. F. Coker, and A. H. C. Neto, Oxygen Defects in Phosphorene, Phys. Rev. Lett. **114**, 046801 (2015).

[10] R. Fei, A. Faghaninia, R. Soklaski, J.-A. Yan, C. Lo, and L. Yang, Enhanced thermoelectric efficiency via orthogonal electrical and thermal conductances in phosphorene, Nano Lett. **14**, 6393 (2014).

[11] L. C. Gomes, A. Carvalho, and A. H. Castro Neto, Enhanced piezoelectricity and modified dielectric screening of two-dimensional group-IV monochalcogenides, Phys. Rev. B **92**, 214103 (2015).

[12] C. Li, L. Huang, G. P. Snigdha, Y. Yu, and L. Cao, Role of boundary layer diffusion in vapor deposition growth of chalcogenide nanosheets: The case of GeS, ACS Nano **6**, 8868 (2012).

[13] J. R. Brent, D. J. Lewis, T. Lorenz, E. A. Lewis, N. Savjani, S. J. Haigh, G. Seifert, B. Derby, and P. O'Brien, Tin(II) sulfide (SnS) nanosheets by liquid-phase exfoliation of herzenbergite: IV-VI main group two-dimensional atomic crystals, J. Am. Chem. Soc. **137**, 12689 (2015).

[14] A. Ziletti, A. Carvalho, P. E. Trevisanutto, D. K. Campbell, D. F. Coker, and A. H. Castro Neto, Phosphorene oxides: Bandgap engineering of phosphorene by oxidation, Phys. Rev. B **91**, 085407 (2015).

[15] R. A. Doganov, E. C. T. O'Farrell, S. P. Koenig, Y. Yeo, A. Ziletti, A. Carvalho, D. K. Campbell, D. F. Coker, K. Watanabe, T. Taniguchi, A. H. Castro Neto, and B. Özyilmaz, Transport properties of pristine few-layer black phosphorus by van der Waals passivation in an inert atmosphere, Nat. Commun. **6**, 6647 (2015).

[16] A. Avsar, I. J. Vera-Marun, J. Y. Tan, K. Watanabe, T. Taniguchi, A. H. Castro Neto, and B. Özyilmaz, Air-stable transport in graphene-contacted, fully encapsulated ultrathin black phosphorus-based field-effect transistors, ACS Nano **9**, 4138 (2015).

[17] W. Zhu, M. N. Yogeesh, S. Yang, S. H. Aldave, J.-S. Kim, S. Sonde, L. Tao, N. Lu, and D. Akinwande, Flexible black phosphorus ambipolar transistors, circuits and AM demodulator, Nano Lett. **15**, 1883 (2015).

[18] W. Kohn and L. J. Sham, Self-consistent equations including exchange and correlation effects, Phys. Rev. **140**, A1133 (1965).

[19] P. Giannozzi *et al.*, Quantum ESPRESSO: A modular and open-source software project for quantum simulations of materials, J. Phys. Condens. Matter **21**, 395502 (2009).

[20] J. P. Perdew, K. Burke, and M. Ernzerhof, Generalized Gradient Approximation Made Simple, Phys. Rev. Lett. **77**, 3865 (1996).

[21] N. Troullier and J. L. Martins, Efficient pseudopotentials for plane-wave calculations, Phys. Rev. B **43**, 1993 (1991).

[22] H. J. Monkhorst and J. D. Pack, Special points for Brillouin-zone integrations, Phys. Rev. B **13**, 5188 (1976).

[23] H. Wiedemeier and H. G. Schnering, The high temperature structure of β-SnS and β-SnSe and the B16-to-B33 type λ-transition path, Z. Kristallogr. **156**, 143 (1981).

[24] L. Ehm, K. Knorr, P. Dera, A. Krimmel, P. Bouvier, and M. Mezouar, Pressure-induced structural phase transition in the IV-VI semiconductor SnS, J. Phys. Condens. Matter **16**, 3545 (2004).

[25] I. Lefebvre, M. A. Szymanski, J. Olivier-Fourcade, and J. C. Jumas, Electronic structure of tin monochalcogenides from SnO to SnTe, Phys. Rev. B **58**, 1896 (1998).

[26] J. P. Goss, M. J. Shaw, and P. R. Briddon, Marker-method calculations for electrical levels using gaussian-orbital basis sets, *Theory of Defects in Semiconductors*, Volume 104 of the series Topics in Applied Physics (Springer, Berlin, Heidelberg, 2016), pp. 69–94.

[27] A. Carvalho and A. H. Castro Neto, Donor and acceptor levels in semiconducting transition-metal dichalcogenides, Phys. Rev. B **89**, 081406 (2014).

[28] J. Vidal, S. Lany, M. d'Avezac, A. Zunger, A. Zakutayev, J. Francis, and J. Tate, Band-structure, optical properties, and defect physics of the photovoltaic semiconductor SnS, Appl. Phys. Lett. **100**, 032104 (2012).

[29] A. J. Jackson, D. Tiana, and A. Walsh, A universal chemical potential for sulfur vapours, Chem. Sci. **7**, 1082 (2016).

[30] O. K. Al-Mushadani and R. J. Needs, Free-energy calculations of intrinsic point defects in silicon, Phys. Rev. B **68**, 235205 (2003).

[31] S. K. Estreicher, M. Sanati, D. West, and F. Ruymgaart, Thermodynamics of impurities in semiconductors, Phys. Rev. B **70**, 125209 (2004).

[32] A. Carvalho, R. Jones, M. Sanati, S. K. Estreicher, J. Coutinho, and P. R. Briddon, First-principles investigation of a bistable boron-oxygen interstitial pair in Si, Phys. Rev. B **73**, 245210 (2006).

[33] M. Sanati and S. K. Estreicher, First-principles thermodynamics of defects in semiconductors, Physica B (Amsterdam) **340-342**, 630 (2003).

[34] A. Gali, J. E. Lowther, and P. Deák, Defect states of substitutional oxygen in diamond, J. Phys. Condens. Matter **13**, 11607 (2001).

[35] A. F. Wright, Substitutional and interstitial oxygen in wurtzite GaN, J. Appl. Phys. **98**, 103531 (2005).

[36] A. Chroneos, E. N. Sgourou, C. A. Londos, and U. Schwingenschlgl, Oxygen defect processes in silicon and silicon germanium, Appl. Phys. Rev. **2**, 021306 (2015).

[37] G. A. Tritsaris, B. D. Malone, and E. Kaxiras, Structural stability and electronic properties of low-index surfaces of SnS, J. Appl. Phys. **115**, 173702 (2014).

[38] J. Lu, A. Carvalho, X. K. Chan, H. Liu, B. Liu, E. S. Tok, K. P. Loh, A. H. Castro Neto, and C. H. Sow, Atomic healing of defects in transition metal dichalcogenides, Nano Lett. **15**, 3524 (2015).

[39] Y. Liu, P. Stradins, and S.-H. Wei, Air passivation of chalcogen vacancies in two-dimensional semiconductors, Angew. Chem., Int. Ed. Engl. **55**, 965 (2016).